Int. J. Electrochem. Sci., 13 **(2018)** 6693 – 6707, doi: 10.20964/2018.07.45

International Journal of ELECTROCHEMICAL SCIENCE
www.electrochemsci.org

Synthesis and Characterization of Cu_2CdSnS_4 Quaternary Alloy Nanostructures

Y. Al-Douri[1,2,*], *Ali Abu Odeh*[3], *Mohd Rafie Johan*[1], *Zaira Zaman Chowdhury*[1], *Rahman F. Rafique*[4], *Ali H. Reshak*[5], *C. H. Voon*[6]

[1] Nanotechnology and Catalysis Research Center (NANOCAT), University of Malaya, 50603 Kuala Lumpur, Malaysia
[2] Physics Department, Faculty of Science, University of Sidi-Bel-Abbes, 22000-Algeria
[3] Khawarizmi International College, 68297-Al Ain, United Arab Emirates
[4] Rutgers Cooperative Extension Water Resources Program, The State University of New Jersey, New Brunswick, NJ 08901-8551, USA
[5] New Technologies – Research Center, University of West Bohemia, Univerzitni 8, Pilsen 30614, Czech Republic
[6] Institute of Nano Electronic Engineering, University Malaysia Perlis, 01000 Kangar, Perlis, Malaysia
[*]E-mail: yaldouri@yahoo.com

Received: 16 January 2018 / *Accepted:* 28 February 2018 / *Published:* 5 June 2018

Cu_2CdSnS_4 (CCTS) quaternary alloy nanostructure is an important material of enhancing the sensors effectiveness. CCTS nanostructures have been synthesized using ultrasonic and deposited on SiO_2/Si substrate using sol-gel method and under annealing temperature; 400 ^oC. Structural optical, topographical and morphological properties of CCTS were explored using Ultraviolet–visible spectroscopy, X-ray diffraction (XRD), atomic force microscopy (AFM) and scanning electron microscopy (SEM), respectively. Interdigitated electrodes (IDEs) have been manufactured via deposited silver on CCTS/SiO_2/Si substrate via a physical vapor deposition and hard mask. Electrical properties of fabricated IDEs are further evaluated as a function of voltage and frequency. The proposed IDEs can be used in subsequent studies to develop a biological sensor capable of detecting the DNA for many types of diseases in order to facilitate the combating and eradicating. The resulted values are in agreement with others.

Keywords: Cu_2CdSnS_4; Nanostructures; Optical; Structural; Electrical.

1. INTRODUCTION

Due to high request of effective and accurate sensors, research is ongoing for new elements and methods to design and build biosensors that are based on capacitive electrodes. Common capacitive

structures such as parallel plate and interdigitated electrodes (IDEs) are used widely in the literature, the first is distinguished by unpretentious design in terms of modeling [1], whereas, the second is more favored due to its effectiveness in acquiring stable and fixed temperature for the dielectric [2]. Four different electrodes models discussed thoroughly in the literature can be used as some capacitive sensors; interdigitated electrodes, spiral electrodes, meandered electrodes and serpentine electrodes. IDEs are considered for sensing; the signals have been detected by sensing materials. Analytical equations for the capacitance between electrodes fingers have been developed, which proposed a general model that can be used for any dimension and finger width as well as any number of layers with different permittivity and thickness [3]. The geometry of interdigitated schottky-barrier has been enhanced thus, the quantum efficiency and response time are analyzed and the optimum spacing for interdigitated photodetector has been identified [4]. The process of IDEs manufacturing consists of different steps of exposure, photoresist coating and etching processes using special instruments [5-10]. Therefore, many attempts have been done for simplifying the fabrication process by introducing some new and different ones such as inkjet-printing [11-13], screen printing [14], micro fabrication [15] and stamp method [16]. IDEs have been explored extensively and used widely in many applications such as humidity sensing [17], gas sensing [18], bacteria sensing [19], pressure sensing [20], DNA sensing [21], pH sensing [22] and immunosensor [23].

Copper-based quaternary I_2−II− IV−VI_4 chalcogenide semiconductors have attracted intensive interest due to their composition of abundant elements that have high optical and structural characteristics useful for many applications such as photovoltaics and biosensors. A pollution-free process for synthesizing Cu_2ZnSnS_4 (CZTS) using a hydrazine-free solvothermal approach and synthesizing $Cu_2ZnSn(S,Se)_4$ (CZTSSe) counter electrodes (CEs) in dye-sensitized solar cells (DSCs) have been developed. DSCs fabricated with CZTSSe CEs have attained a higher power conversion efficiency than of cell uses CZTS CEs in fabrication process [24]. A limited number of research papers have explored Cu_2CdSnS_4 (CCTS) and a few number of techniques has been utilized to prepare it such as solvothermal [25,26], microwave irradiation [27], facile synthesis [28], chemical bath deposition [29], spray pyrolysis deposition [30] and co-sputtering deposition [31]. $Cu_2Zn_{1-x}Cd_xSnS_4$ quinternary alloy nanostructures have deposited on oxidized silicon substrate at multiple Cd concentrations (x = 0. 0.2, 0.4, 0.6, 0.8, 1) via sol-gel method. The resulted nanostructures were functionalized with oligonucleotides probe DNA molecules from cervical cancer and interacted with the target DNA, exhibiting good sensing capabilities. The immobilization and hybridization processes were analyzed via representative current-voltage (I-V) plot, moreover, its electrical profile shows that the device is capable to distinguish biomolecules [32]. Using ultrasonic in synthesizing CCTS via spin coating technique leads to introducing more peaks. Moreover, applying high annealing temperatures will increase the crystallite size [33].

In this work, CCTS was prepared and then deposited on SiO_2/Si using sol-gel method at annealing temperature; 400 °C. In addition, the optical, crystallite structures and morphology of CCTS were investigated in detail. The design and fabrication of IDEs have been elaborated, furthermore, their electrical properties have been characterized. This research is arranged as the following; section 2 describes the experimental process, the results and discussion are elaborated in section 3. Lastly, the summary is concluded in section 4.

2. EXPERIMENTAL

2.1. Synthesis of CCTS solution

The solution was produced from copper (II) chloride dihydrate ($CuCl_2.2H_2O$) (0.6 M), tin (II) chloride dihydrate ($SnCl_2.2H_2O$) (0.8 M), cadmium (II) chloride dihydrate ($CdCl_2.2H_2O$) (0.8 M), thiourea (CH_4N_2S) (0.8 M), 2-methoxyethanol ($C_3H_8O_2$) and monoethanolamine (C_2H_7NO) were all of analytical grade and purchased from Sigma-Aldrich. The stabilizer and solvent were 2- ethanolamine and methoxyethanol, respectively. The molar ratio of S, Sn, Cd and Cu in the solution was 4:1:1:2. The specified molar concentrations of the precursors were identified using the following equations;

$$Molarity\ (M) = \frac{n}{V} \quad (1)$$

$$n = \frac{m(g)}{M_m\,(g/mol)} \quad (2)$$

where n is moles of solute, V is liters of solution, m is mass (g) and M_m is molecular mass (g/mol). The precursors were mixed using a magnetic stirrer (WiseStir MSH 30D) at a speed of 1500 RPM for 3 hours, and temperature, 50 °C which results into a yellowish solution. The resulted solution has been placed inside the ultrasonic cleaner (DELTA DC200H) for 30 minutes at 50 °C to boost the physical and chemical properties of the solution.

2.2. Deposition of the solution via sol-gel method

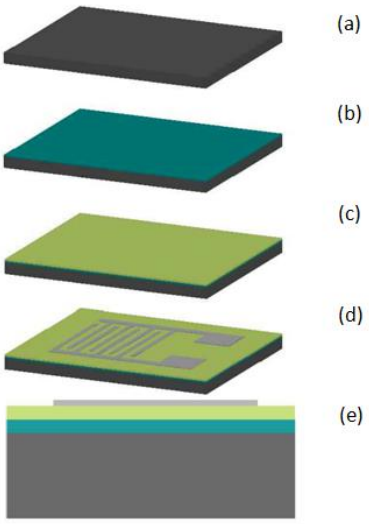

Figure 1. Schematic illustration of IDEs fabrication steps (a) Si substrate (b) SiO_2/Si, (c) CCTS/SiO_2/Si, (d) Ag/CCTS/SiO_2/Si, (e) cross section view of the sample.

n-Si wafer with orientation <100> was washed by immersing in RCA 1 and RCA 2 solutions successively to omit metallic, ionic and residual organic contamination as displayed in Fig. 1a. Si substrate was oxidized which resulted in forming silicon oxides by exposing it to temperature, 1000 °C under O_2 gas flow for 1 h via diffusion furnace (MODU-LAB) as displayed in Fig. 1b. Then, the resulted substrate has been placed inside the spin coater (Laurell WS-400B) where, some drops of the

prepared solution was dropped on the substrate. The rotation speed of the spin coater was 1500 RPM for 30 sec for depositing the solution uniformly on the substrate. The spin coating was followed directly by drying the substrate on the hot plate for 1 min at 80 °C. The sol-gel and drying were iterated several times to gain steady layer of CCTS with adequate thickness upon SiO_2/Si as illustrated in Fig. 1c. Furthermore, the annealing process took place for 1 hour at temperature, 400 °C [33,34] with the flow of N_2 gas, then, it has been left intact to cool down.

2.3. Fabrication of IDEs

To fabricate some effective IDEs, chrome mask made since it is much better than conventional lithographic technique because it requires less steps and instruments. Ag is used for deposition of IDEs since it is the highest electric conductive element among the others. The deposited electrodes have a thickness, 100 nm using physical vapor deposition (PVD) as depicted in Fig. 1d. Basing on PVD machine specifications, to identify thickness according to raw silver weight utilized, a correlation between silver weight and thickness of IDEs is fixed. The IDEs thickness was measured on PVD indicator. The four layers cross section of Ag/CCTS/SiO_2/Si is depicted in Fig. 1e.

The optical characteristic has been examined via Ultraviolet–visible (UV-vis) spectrophotometer (Perkin Elmer Lambda 35) using wavelength, 200 - 1000 nm to identify energy gap. The structural characteristics have been explored via X-ray diffractometer (XRD) (D2 PHASER, BRUKER), the Bragg's angle (2θ) range was 10^o- 60° at a rate, 5^o/min. The resulted peaks have registration, referred to compatible planes. Atomic Force Microscopy (AFM) (SPA 400, Seiko Instruments Inc.) to identify topography with an active area of 5 μm x 5 μm and rate, 1 Hz whereas, Scanning Electron Microscopy (SEM) (JSM-6010LV) to explore morphology with a magnification factor, x5000. Electricals of IDEs were characterized using (KEITHLEY 6487, Tektronix) and (Alpha-A High Performance Modular Measurement System, novocontrol).

3. RESULTS AND DISCUSSION

3.1 CCTS Analysis and characterization

3.1.1 Optical properties

Reflection versus wavelength was conducted using UV-vis spectroscopy at the range, 200-1000 nm. In agreement with Tauc equation [35] for determining the optical band gap, that can be determined;

$$(\alpha h\nu)^2 = A(h\nu - E_g) \quad (3)$$

where α is absorption coefficient, A is constant, E_g is band gap, ν is incident frequency and h is Planck's constant. Tauc's region is extrapolated to $(\alpha h\nu)^2 = 0$ to obtain the energy gap as displayed in Fig. 2. The band gap is 1.35 eV, that is close to the available data in the literature [33,34] and an impetus to employ CCTS in photovoltaics and biosensors.

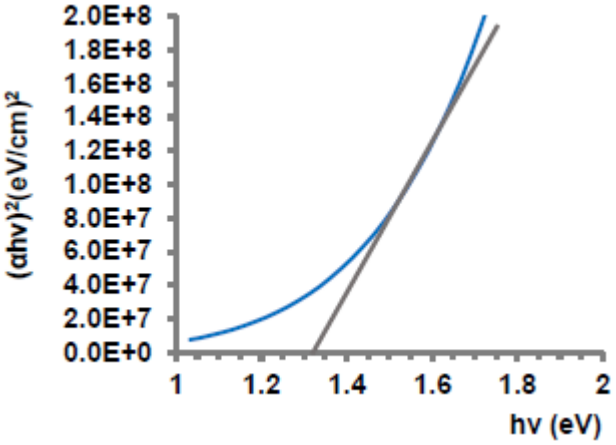

Figure 2. $(\alpha hv)^2$ versus hv of CCTS quaternary alloy nanostructures deposited on SiO_2/Si substrate.

The main observation is observed from Fig. 2, the reflection spectra is at ambient temperature. It is noticed that the reflection level is determined. The deduced band gap is in good agreement with the reported values [33,34]. The band gap is quite close to the optimum band gap, which indicates that CCTS quaternary alloy nanostructure is promising materials for photovoltaic applications.

The refractive index *n* is a very important physical parameter related to the microscopic atomic interactions. From theoretical view point, there are basically two different approaches of viewing this subject: the refractive index will be related to the density and the local polarizability of these entities [36]. Consequently, many attempts have been made in order to relate the refractive index and the energy gap E_g through simple relationships [37-42]. However, these relations of *n* are independent of temperature and incident photon energy. Here the various relations between *n* and E_g will be reviewed. Ravindra et al. [42] had presented a linear form of *n* as a function of E_g:

$$n = \alpha + \beta E_g \tag{4}$$

where $\alpha = 4.048$ and $\beta = -0.62$ eV^{-1}. Light refraction and dispersion will be inspired. Herve and Vandamme [43] have proposed an empirical relation as follows:

$$n = \sqrt{1 + \left(\frac{A}{E_g + B}\right)^2} \tag{5}$$

where $A = 13.6$ eV and $B = 3.4$ eV. For group-IV semiconductors, Ghosh et al. [44] have published an empirical relationship based on the band structure and quantum dielectric considerations of Penn [45] and Van Vechten [46]:

$$n^2 - 1 = \frac{A}{(E_g + B)^2} \tag{6}$$

where $A = 8.2E_g + 134$, $B = 0.225E_g + 2.25$ and $(E_g + B)$ refers to an appropriate average energy gap of the material. The calculated refractive indices of the end-point compounds are listed in Table 1. This is verified by the calculation of the optical dielectric constant ε_∞ which depends on the refractive index. Note that $\varepsilon_\infty = n^2$ [47]. It is clear that the investigated refractive index calculated by the model of Herve and Vandamme [43] is agreed well for CCTS quaternary alloy nanostructure in

enhancing the photo conversion. It means high absorption and low reflection may be attributed to increase devices efficiency.

3.1.2 Structural properties

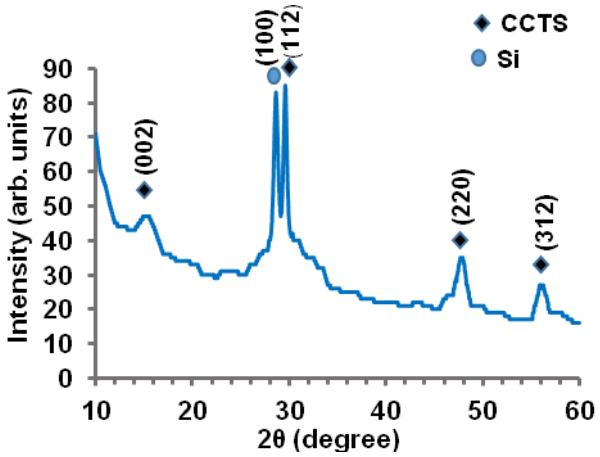

Figure 3. XRD pattern of CCTS quaternary alloy nanostructures deposited on SiO_2/Si substrate.

CCTS has been explored by X-ray diffraction as displayed in Fig. 3. XRD provides information for phase identification and unit cell dimensions of crystallite material. By examining the pattern, five main diffraction peaks existed at 2θ = 16.2091°, 28.6133°, 29.576°, 47.7728° and 55.9574 were referred to (002), (111), (112), (220) and (311) planes, respectively. In this study, the structure of CCTS belongs to the tetragonal crystal system and stannite structure that is in agreement with the standard (ICDD PDF2008, 00-029-0537). The lattice constants (a & c) with other parameters are determined from (112) peak as shown in Table 1.

Table 1. The structural parameters of CCTS quaternary alloy nanostructures using XRD.

Crystallite size (D) (nm)	Lattice constants a and c (Å)	Strain (10^{-3})	Dislocation density (10^{14})	N/area (10^{15})	Thickness (nm)
26.8	a=5.52 c=10.91 a=5.48 c=10.84[a] a=5.46 c=10.48[b]	0.086	19.17	6	54

[a] Ref. [30] Theo.; [b] Ref. [38] Theo.

The interplanar distance (d) was calculated via Bragg's law [48];

$$d = \frac{n\lambda}{2sin(\theta)} \quad (7)$$

where λ is wavelength (λ = 1.5406 Å) and θ is Bragg's angle.

Lattice constants (a & c) were determined from X-ray diffraction pattern using the equation below;

$$\frac{1}{a^2} = \frac{h^2+k^2}{a^2} + \frac{l^2}{c^2} \quad (8)$$

where *hkl* is Miller indices. By joining equations (7) and (8), *a* and *c* constants can be determined in terms of *sin θ*.

$$sin^2\theta = \frac{\lambda^2}{4a^2}(h^2 + k^2) + \frac{\lambda^2}{4c^2}(l^2) \quad (9)$$

The crystallite size (D) was determined using Scherrer's formula [49];

$$D = \frac{k\,\lambda}{\beta cos(\theta)} \quad (10)$$

where *k* is constant equals 0.94, and *β* is FWHM of major peak (radian). Table 1 presents dislocation density (δ), number of crystallites per unit area (*N*) and strain (ε).

$$\delta = \frac{1}{D^2} \quad (11)$$

$$\varepsilon = \frac{\beta cos\theta}{4} \quad (12)$$

$$N = \frac{t}{D^3} \quad (13)$$

where *t* is the thickness as mentioned in Table 1.

It is deduced that the highest peak (Fig. 3) is the optimum to be applied in photovoltaics and biosensors that give high sensitivity and marvelous results due to nanosized particle and thickness attributed to quantum confinement principle. The lattice constants a and c were calculated from XRD patterns of (112) plane, using the equations (7-13) according to the tetragonal crystal system.

It is known that the bulk modulus is a reflectance of the materials stiffness that it is important in different industries. Many authors [50-55] have made various efforts to explore thermodynamic properties of solids. In these studies, authors have examined the thermodynamic properties such as the inter-atomic separation and the bulk modulus of solids with different approximations and best-fit relations [52-55]. It has become possible to compute with great accuracy an important number of structural and electronic properties of solids. The *ab initio* calculations are complex and require significant effort. Therefore, more empirical approaches have been developed [56,57] to compute properties of materials. In many cases, the empirical methods offer the advantage of applicability to a broad class of materials and to illustrate trends. In many applications, these empirical approaches do not give highly accurate results for each specific material, but are still very useful. Cohen [58] has established an empirical formula for calculation of the bulk modulus B_0; based on the nearest-neighbor distance. Lam et al. [59] have derived an analytical expression for the bulk modulus from the total energy. This expression is different in structure from the empirical formula but gives similar numerical results. Also, they have obtained an analytical expression for the pressure derivative B_0 of the bulk modulus. Our group [60] have used a concept based on the lattice constant to establish an empirical formula for the calculation of the bulk modulus. The investigated results are presented. Consideration of hypothetical structure and simulation of the experimental conditions are required to make practical use of this formula. To see how a qualitative concept, such as the bulk modulus, can be related to the lattice constant, it was argued that the dominant effect is the degree of covalency characterized by Phillips' homopolar gap E_h [56], and one reason for presenting these data in this work is that the validity of our calculations that is not restricted in computed space. We thus believe that the data will

prove valuable for future work in this field. An important reason for studying B_0 is the observation of clear differences between the lattice constants for CCTS quaternary alloy nanostructure as seen in Table 1. The basis of our model is the lattice constant as seen in Table 1. Fitting of these data gives the following empirical formula [61]:

$$B_0 = [3000 - 100\lambda]\left(\frac{a}{2}\right)^{-3.5} \quad (14)$$

where a is the lattice constant (in Å) and λ is an empirical parameter; λ = 0; 1, 2 for group IV, III–V, and II–VI semiconductors, respectively. In Table 1, the calculated bulk modulus value is investigated. We may conclude and that the calculated bulk modulus exhibits the same chemical trends as those found elsewhere in the literature.

3.1.3 Topography and morphology

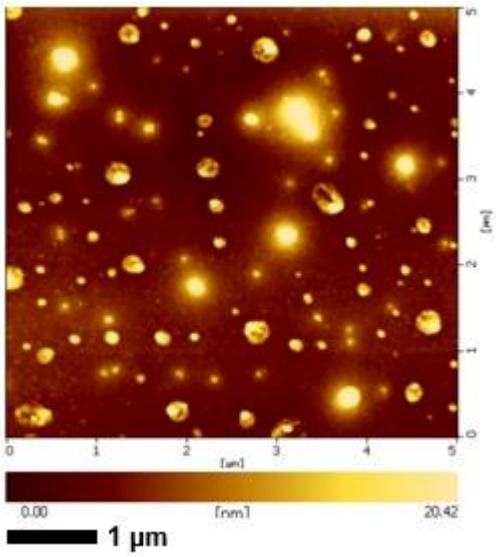

Figure 4. 2D AFM image of CCTS quaternary alloy nanostructures deposited on SiO_2/Si substrate.

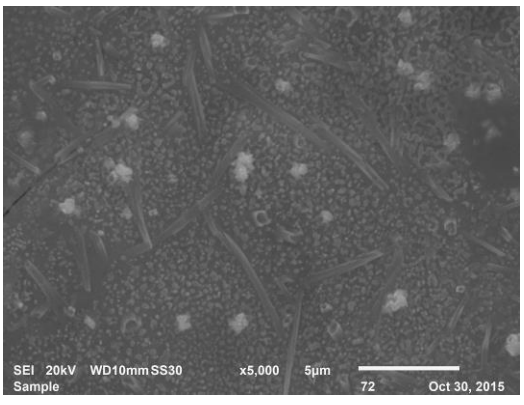

Figure 5. SEM image of CCTS quaternary alloy nanostructures deposited on SiO_2/Si substrate.

The topography has been characterized. Figure 4 illustrates 2-D AFM image with an area, 5 μm x 5 μm at a rate, 1 Hz and roughness, 1.95 nm. The SEM given in Fig. 5 is described the morphology. The nearby look displays dense morphology, uniform with some grains. It is noticed that Cu represents white spots of topography that characterizes the nature of surface including locations of different elements (Fig. 4). Otherside, the shape of quaternary alloy deposited on Si shows its morphology that supports possibility of photovoltaics and biosensors manufacturing.

The roughness has factors connected to diffusion, substrate, temperature and spin coating speed. The deposition at ambient temperature does not show robust structure, but it seems more scattered and blurring. Furthermore, tiny spots can be noticed. Therefore, the morphology is found to be homogenous grained structures that can be seen, and in agreement with particle size obtained from X-ray diffraction (Table 1).

A closer look with morphology image, the deposition does not exhibit a robust structure, and it looks more blurring and scattered. Moreover, small cavities can be seen. However, the morphology is found to be improved and cohesive layer of grained structures can be observed and is in accordance with crystallite size estimated from XRD pattern in Table 1.

3.2 Electrical properties of IDEs

Ag IDEs deposited onto CCTS/SiO_2/Si substrate using PVD created IDEs pair with four fingers each. The IDEs comprised 8 fingers with 0.25 mm wide (W), 3.75 mm long (L) with 0.25 mm gap (G) between two adjacent IDEs. Furthermore, the fingers thickness is 100 nm and wavelength λ equals 1 mm as shown in Fig. 6a. Lastly, photograph of Fig. 6b is shown.

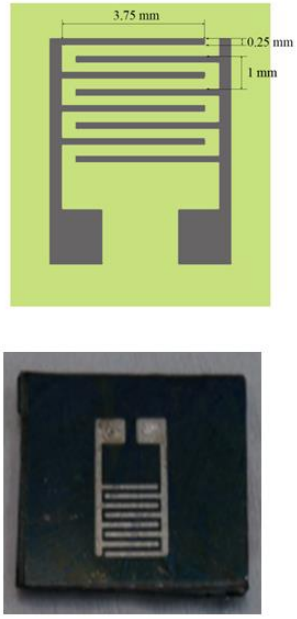

Figure 6. Images of fabricated IDEs (a) layout of IDEs plane and dimensions and (b) photograph of the whole sample.

Electricals of IDEs have been investigated via KEITHLEY 6487 with two-point probes as shown in Fig. 7. Within applied voltage ranging from -5 to 5 V, the resulted current through the device increases from -10 nA to 10 nA with semilinear relationship as shown in Fig. 7a. This behavior is identified as Schottky barrier, which is formed in a metal–semiconductor junction. IDEs have metallic electrodes on Si substrate with a thin insulator of O_2 between them, Therefore, I–V curves show specific currents at zero V; due to charging effect on electrical double existence and capacitance of CCTS quaternary nanostructures between IDEs and O_2 layer. Resistance (R) is calculated using ohm's law.

$$R = V/I \quad (15)$$

where V is voltage and I is current. Resistance versus voltage is shown in Fig. 7b, the resistance was 0.427 GΩ at -5 V and its fluctuated slightly until the applied voltage reached -0.7 V, where resistance ramped up to 17.6 GΩ and then ramped down to -4 GΩ.

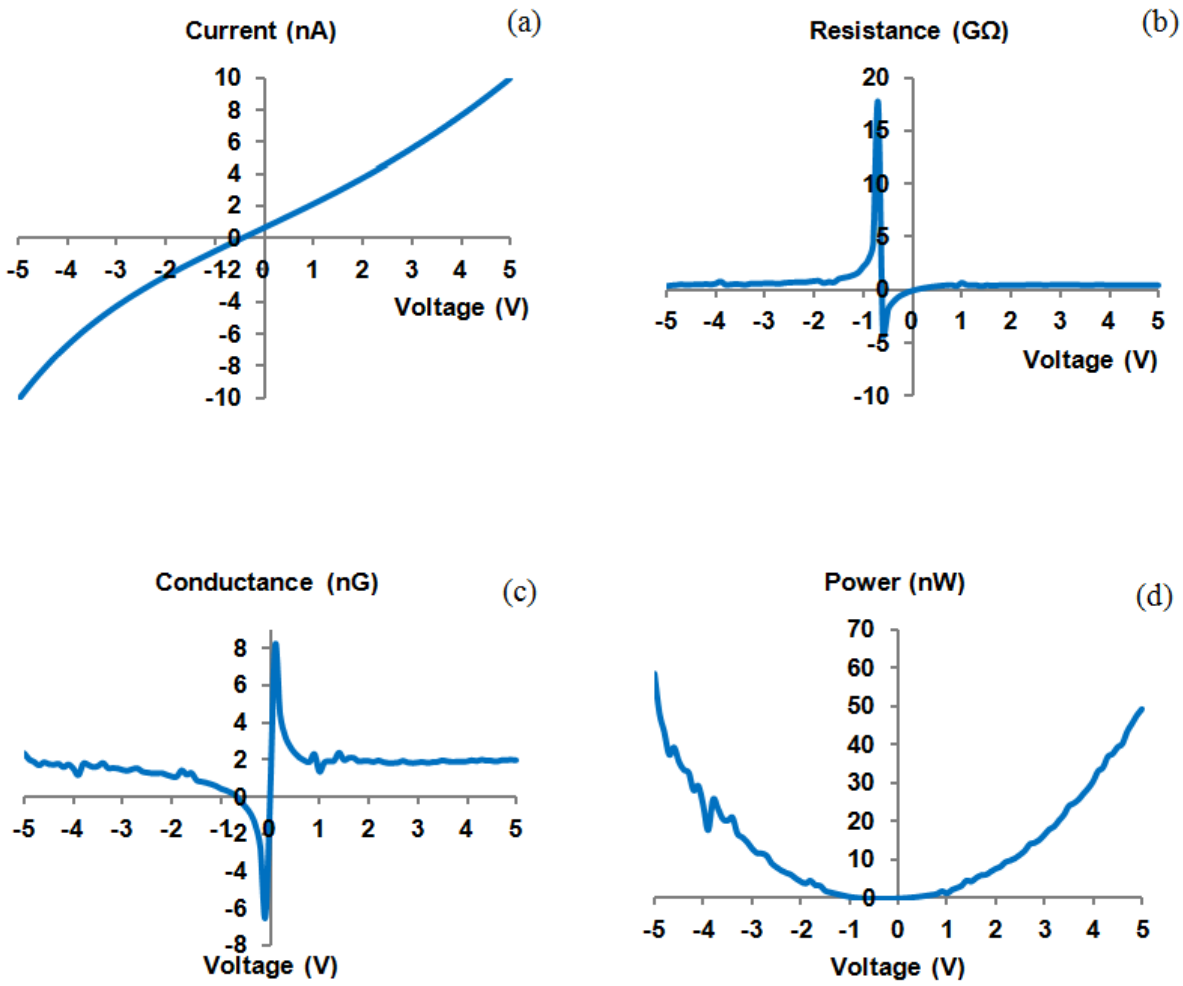

Figure 7. Electrical characteristics of IDEs using KEITHLEY 6487 as a function of voltage(a) current versus voltage (I-V), (b) resistance versus voltage, (c) conductance versus voltage and (d) power versus voltage.

The recorded resistance was 0.5 GΩ at 5 V. It is noticed that the unstable resistance region is falling between -1.5 V and -0.4 V. It is worth mentioning, when the gap increases, the resistance increases that is attributed to carriers of charge have long distance to travel. On the other hand, conductance is the reciprocal of the resistance, it can be observed that conductance has the same behavior as resistance but in opposite way as shown in Fig. 7c. Electrical power (P) is resulted from multiplying voltage with current, power was 58 nW at -5 V and continue to decrease to 0 W at 0 V followed by power increases to 50 nW at 5 V as shown in Fig. 7d. This is recommended for high sensitivity for nanotechnological applications, especially conductance and resistance are confirmed, and supported by measured power of device noiseless.

Further measurements were used Alpha-A for different parameters in terms of frequency. The capacitance (C) is calculated using the following;

$$C = \varepsilon_r \varepsilon_0 A/d \quad (16)$$

where ε_r is the relative static permittivity of material between the fingers, ε_0 is the constant permittivity of air ($\varepsilon_0 \approx 8.854\times10^{-12}$ F·m^{-1}), A is the area of the electrode and d is the separation distance between the fingers.

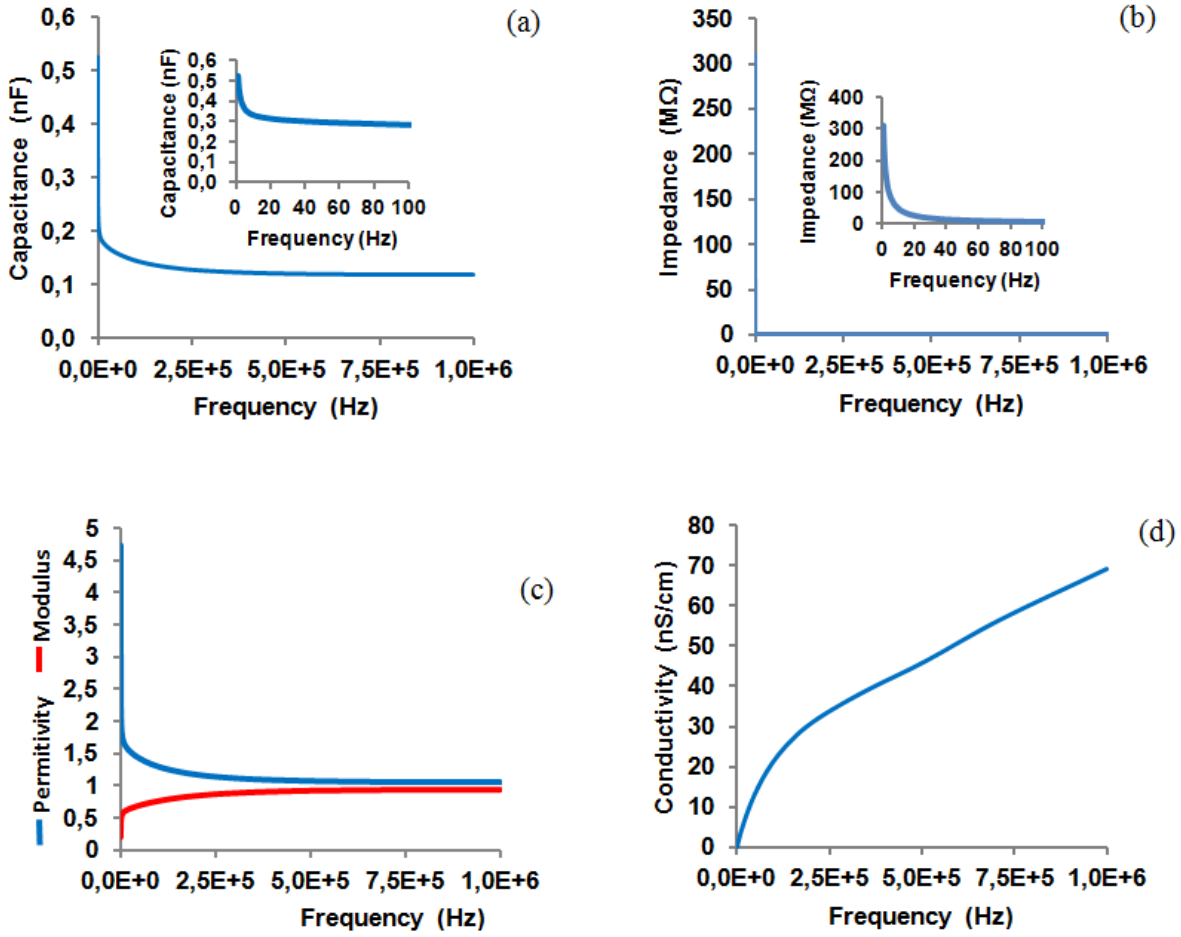

Figure 8. Electrical characteristics of IDEs using Alpha-A analyzer as a function of frequency (a) capacitance versus frequency (I-V), (b) impedance versus frequency, (c) permittivity and modulus versus frequency and (d) conductivity versus frequency. The insets in a and b shows the frequency trend in the first 100 Hz.

Figure 8a shows the capacitance of IDEs in terms of frequency, the capacitance was 0.12 nF at 1 MHz and increasing dramatically as frequency decreases until it reaches 0.52 nF at 1 Hz, hence, there is inversely relationship between capacitance and frequency. Despite the current figures, increasing the number of fingers and the thickness of the electrodes will lead to increasing the capacitance. Otherside, impedance is a measure of opposition at applied voltage. Impedance phase and magnitude, unlike resistance, has a magnitude. The capacitors impedance (*Zc*) is calculated using;

$$Zc = \frac{1}{jwC} \quad (17)$$

where *j* is the imaginary part, *w* is the omega which has a unit of radian per sec and equals $2\pi f$. Figure 8b shows the impedance of IDEs as a function of frequency, it was 34 KΩ at 1 MHz and increasing dramatically as frequency decreases until it reaches 310 MΩ at 1 Hz.

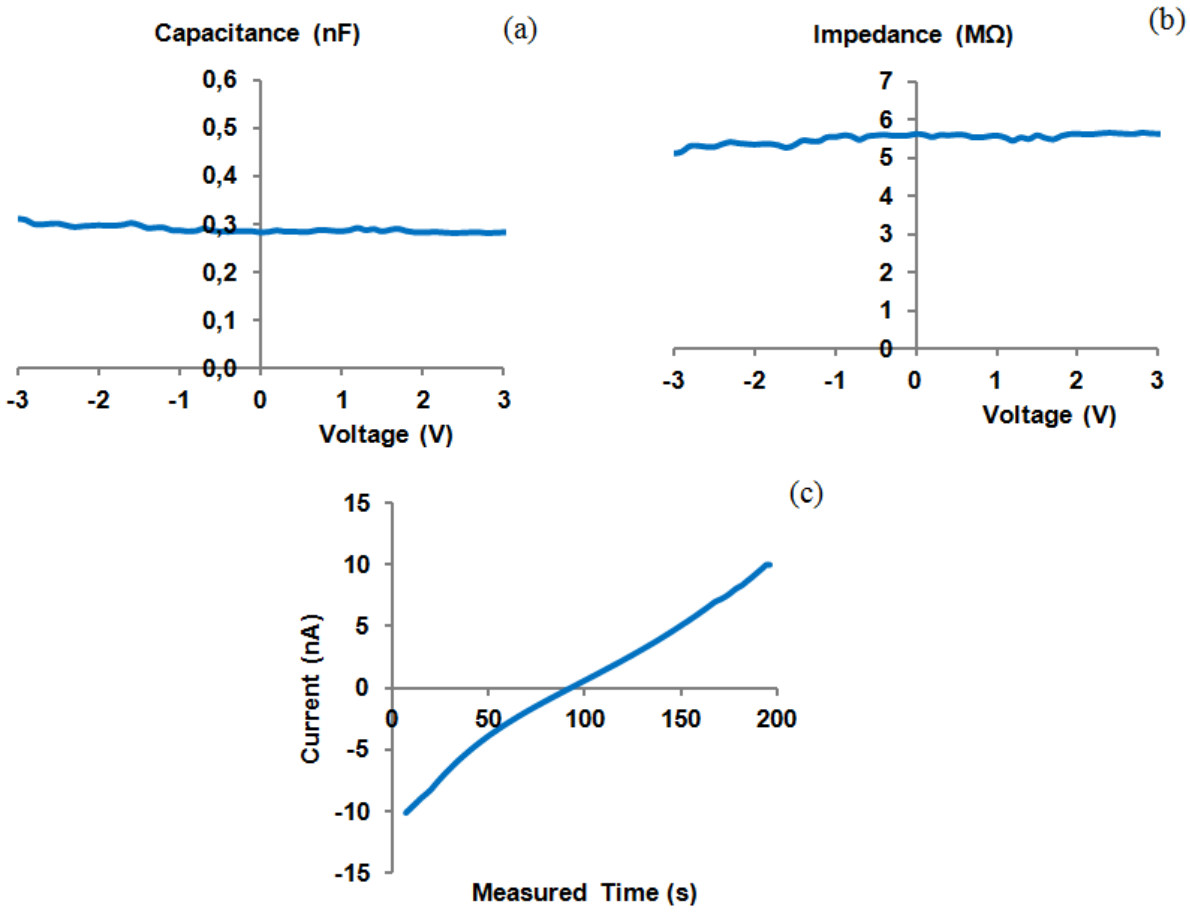

Figure 9. Electrical characteristics of IDEs using Alpha-A analyzer as a function of voltage and time (a) capacitance versus voltage (I-V), (b) impedance versus voltage and (c) current versus measured time.

Therefore, impedance increases as frequency decreases with inversely relationship. Permittivity (ε) is a measure of how an electric field affects, and is affected by, a dielectric medium. It has (F/m) and represented by;

$$\varepsilon = \varepsilon_r \varepsilon_0 \quad (18)$$

Figure 8c shows the permittivity and the modulus of IDEs in terms of frequency, permittivity was 1.07 F/m at 1 MHz and increasing dramatically as frequency decreases until it reaches 4.62 F/m at 1 Hz. Otherside, electric modulus is reciprocal of the permittivity, hence, it was 0.93 m/F at 1 MHz and decreasing dramatically as frequency decreases until it reaches 0.21 m/F at 1 Hz. The electrical resistivity (ρ) is defined as:

$$\rho = R\frac{A}{\ell} \tag{19}$$

where R is the electrical resistance of material, ℓ is the length of the material and A is the cross-sectional area of material. The electrical conductivity (σ) is defined as the reciprocal of the resistivity and it has (S/m);

$$\sigma = \frac{1}{\rho} \tag{20}$$

Figure 8d illustrates the conductivity of IDEs as a function of frequency, it was 69 nS/m at 1 MHz and continue to decrease as frequency decreases until 0.002 nS/m at 1 Hz. It is known a correlation between impedance and conductivity to let permittivity extends smoothly and verify the punctuality of device measurements for photovoltaics and biosensors.

Additional measurement was done by Alpha-A High to find the impedance and capacitance in terms of voltage. Figure 9a illustrates IDEs capacitance as a function of voltage, it was 0.311 nF at -3 V and continued to fluctuate between 0.2 and 0.3 nF until it reaches 0.283 nF at 3 V. Also, as shown in Fig. 9b, the impedance was 5.11 MΩ at -3 V and ended up with 5.62 MΩ at 3 V. Finally, Fig. 9c shows the current as a function of measured time, the current changes from -10 nA to 10 nA within 190 sec. The study herein was to strengthen a previous work that used CCTS with IDEs for sensing Dengue DNA, CCTS was prepared and deposited on SiO_2/Si using sol-gel method at 400 °C. Ag IDE was fabricated above CCTS/SiO_2/Si via PVD machine and hard mask. The biosensor's sensitivity was calculated to be 24.2 µA nM^{-1} cm^{-2}, while the limit of detection (LOD) and limit of quantification (LOQ) were 16.9 and 56.3 nM, respectively [62].

4. CONCLUSIONS

CCTS nanostructure has been prepared successfully and deposited on SiO_2/Si via sol-gel method at 400 °C. UV-vis has demonstrated band gap, 1.35 eV. X-ray diffraction pattern has showed five peaks; (112) plane is attributed to the highest one whereas, particle size was 26.8 nm. Topography and morphology have indicated the nanostructures coherency and homogeneity as shown in AFM and SEM images, respectively. The roughness was 1.95 nm. Ag IDE was fabricated on CCTS/SiO_2/Si via PVD and hard mask. The model of Herve and Vandamme is agreed well for CCTS quaternary alloy nanostructure. Also, the investigated bulk modulus exhibits the same chemical trends as those found elsewhere in the literature. As seen in electrical measurements, there is a proportional relationship between I and V which is interpreted as Schottky barrier. Otherside, impedance and capacitance measurements have showed inversely correlation with frequency, where they are slightly affected with voltage change. Furthermore, device conductivity increases as frequency increases. These results indicated that Ag IDEs deposited on CCTS/SiO_2/Si using PVD and hard mask have showed good

sensing capabilities and it can be used as biosensor for detecting different types of DNA in future studies.

References

1. A. Rivadeneyra, J. Fernández-Salmerón, M. Agudo-Acemel, J. A. López-Villanueva, L. F. Capitan-Vallvey, A. J. Palma, *Sens. Actu., A: Phys.* 244 (2016) 56.
2. M.Y. El-Naggar, K. Dayal, D. G. Goodwin, K. Bhattacharya, *J. App. Phys.,* 100 (2006) 114115.
3. R. Igreja, C. J. Dias, *Sens. Actu. A: Phys.,* 172 (2004) 392.
4. S. V. Averine, Y. C. Chan, Y. L. Lam, *Solid State Electro.,* 45 (2001) 441.
5. O. P. Singh, N. Muhunthan, K. S. Gour, R. Parmar, M. Dalai, P. Kulriya, S. Pillai, V.N. Singh, *Mater. Sci. Semi. Proces.,* 52 (2016) 38.
6. J. Hong, D .S. Yoon, S. K. Kim, T. S. Kim, S. Kim, E. Y. Pak, K. No, *Lab on a Chip,* 5 (2005) 270.
7. L. Moreno-Hagelsieb, B. Foultier, G. Laurent, R. Pampin, J. Remacle, J. P. Raskin, D. Flandre, *Biosen. Bioelectro.,* 22 (2007) 2199.
8. F. Aslan, A. Göktaş, A. Tumbul, *Mater. Sci. Semi. Proces.,* 43 (2016) 139.
9. M. Pilvet, M. Kauk-Kuusik, M. Altosaar, M. Grossberg, M. Danilson, K. Timmo, A.Mere, V. Mikli, *Thin Solid Films*, 582 (2015) 180.
10. H. W. Jung, Y. W. Chang, G. Y. Lee, S. Cho, M. J. Kang, J. C. Pyun, *Anal. Chim. Acta*, 844 (2014) 27.
11. F. J. Pavinatto, C. W. A. Paschoal, A. C. Arias, *Biosen. Bioelectro.,* 67 (2015) 553.
12. D. D. Le, T. N. N. Nguyen, D. C. T. Doan, T. M. D. Dang, M. C. Dang, *Adv. Nat. Sci.: Nanosci. Nanotech.,* 7 (2016) 025002.
13. A. Rivadeneyra, J. Fernández-Salmerón, M. Agudo, J. A. López-Villanueva, L. F. Capitan-Vallvey, A. J. Palma, *Sens. Actu. B: Chem.,* 195 (2014) 123.
14. L. Manjakkal, K. Cvejin, J. Kulawik, K. Zaraska, D. Szwagierczak, R. P. Socha, *Sens. Actu. B: Chem.*, 204 (2014) 57.
15. Z. Zeng, X. Long, H. Zhou, E. Guo, X. Wang, Z. Hu, *Electrochim. Acta*, 163 (2015) 107.
16. K. Chou, C. Lee, *Adv. Mater. Sci. Eng.*, 2014 (2014) 514508.
17. S. Lei, C. Deng, Y. Chen, Y. Li, *Sens. Actu. A: Phys.,* 167 (2011) 231.
18. A. Brandenburg, J. Kita, A. Groß, R. Moos, *Sens. Actu. B: Chem.,* 189 (2013) 80.
19. M. Mallén-Alberdi, N. Vigués, J. Mas, C. Fernández-Sánchez, A. Baldi, *Sens. Biosen. Res.,* 7 (2016) 100.
20. O. Korostynska, A. Arshak, K. Arshak, D. Morris, *Mater. Sci. Eng. B,* 176 (2011) 1297.
21. X. Fang, Q. Jin, F. Jing, H. Zhang, F. Zhang, *Biosen. Bioelectro.,* 44 (2013) 241.
22. K. Arshak, E. Gill, A. Arshak, O. Korostynska, *Sens. Actu. B: Chem.,* 127 (2007) 42.
23. J. Ahn, T. Han, T. Li, K. Heo, S. Hong, J. Ko, Y. Kim, Y. Shin, M. Kim, *Biosen. Bioelectro.,* 26 (2011) 4690.
24. J. Shen, D. Zhang, J. Li, X. Li, Z. Sun, S. Huang, *Nano-Micro Lett.,* 5 (2013) 281.
25. Y. Cui, G. Wang, D. Pan, *J. Mater. Chem.,* 22 (2012) 12471.
26. M. Cao, L. Li, W. Z. Fan, X. Y. Liu, Y. Sun, Y. Shen, *Chem. Phys. Lett.,* 534 (2012) 34.
27. H. Guan, Y. Shi, H. Hou, X. Wang, F. Yu, *Micro & Nano Lett.,* 9 (2014) 251.
28. C. Li, M. Cao, J. Huang, L. J. Wang, Y. Shen, *Mater. Lett.,* 140 (2015) 170.
29. S. A. Vanalakar, G. L. Agawane, S. W. Shin, M. P. Suryawanshi, K. V. Gurav, K. S. Jeon, P. S. Patil, C. W. Jeong, J. Y. Kim, J. H. Kim, *J. Alloy. Comp.,* 619 (2015) 109.
30. L. Nie, S. Liu, Y. Chai, R. Yuan, *J. Anal. Appl. Pyro.,* 112 (2015) 363.
31. H. Guo, Y. Li, X. Fang, K. Zhang, J. Ding, N. Yuan, *Mater. Lett.,* 162 (2016) 97.
32. A. S. Ibraheam, Y. Al-Douri, C. H. Voon, K. L. Foo, N. Azizah, S. C. B. Gopinath, M. Ameri, S. S. Ibrahim, *Appl. Phys., A* 123 (2017) 123.

33. A. A. Odeh, Y. Al-Douri, R. M. Ayub, A. S. Ibraheam, *J. Alloy. Comp.*, 686 (2016) 883.
34. A. A. Odeh, Y. Al-Douri, R. M. Ayub, M. Ameri, A. Bouhemadou, D. Prakash, K. D. Verma, *Appl. Phys. A*, 122 (2016) 888.
35. Y. Al-Douri, A. H. Reshak, *Optik*, 126 (2015) 5109.
36. N. M. Balzaretti, J.A.H. da Jornada, *Solid State Commun.*, 99 (1996) 943.
37. Y. Al-Douri, H. Khachai, R. Khenata, *Mater. Sci. Semi. Proces.*, 39 (2015) 276.
38. Y. Al-Douri, U. Hashim, R. Khenata, A.H. Reshak, M. Ameri, A. Bouhemadou, A. Rahim Ruslinda, M.K. Md Arshad, *Solar Ener.*, 115 (2015) 33.
39. Y. Al-Douri, Y. P. Feng, A.C.H. Huan, *Solid State Commun.*, 148 (2008) 521.
40. Y. Al-Douri, A. H. Reshak, H. Baaziz, Z. Charifi, R. Khenata, S. Ahmad, U. Hashim, *Solar Ener.*, 84 (2010) 1979.
41. Y. Al-Douri, *Mater. Chem. Phys.*, 82 (2003) 49.
42. N. M. Ravindra, S. Auluck, V.K. Srivastava, *Phys. Stat. Sol. (b)*, 93 (1979) K155.
43. P. J. L. Herve, L. K. J. Vandamme, *J. Appl. Phys.*, 77 (1995) 5476.
44. D. K. Ghosh, L.K. Samanta, G.C. Bhar, *Infrared Phys.*, 24 (1984) 34.
45. D. R. Penn, *Phys. Rev.*, 128 (1962) 2093.
46. J. A. Van Vechten, *Phys. Rev.*, 182 (1969) 891.
47. G. A. Samara, *Phys. Rev. B*, 27 (1983) 3494.
48. Y. Al-Douri, Q. Khasawneh, S. Kiwan, U. Hashim, S. B. Abd Hamid, A. H. Reshak, A. Bouhemadou, M. Ameri, R. Khenata, *Ener. Conver. Manag.*, 82 (2014) 238.
49. A. S. Ibraheam, Y. Al-Douri, U. Hashim, M. Ameri, A. Bouhemadou, R. Khenata, *Microsys. Techno.*, 23 (2017) 2223.
50. A. M. Sherry, M. Kumar, *J. Phys. Chem. Solids*, 52 (1991) 1145.
51. J. L. Tallon, *J. Phys. Chem. Solids*, 41 (1980) 837.
52. M. Kumar, S.P. Upadhyaya, *Phys. Stat. Sol. (b)*, 181 (1994) 55.
53. M. Kumar, *Physica B*, 205 (1995) 175.
54. R. K. Pandey, *J. Phys. Chem. Solids*, 59 (1998) 1157.
55. Q. He, Z-T. Yan, *Phys. Stat. Sol. (b)*, 223 (2001) 767.
56. J. C. Phillips, *Bonds and Bands in Semiconductors*, Academic Press, San Diego, 1973.
57. W. A. Harison, *Electronic Structure and the Properties of Solids*, General Publishing Company, Toronto, 1989.
58. M. L. Cohen, *Phys. Rev. B*, 32 (1985) 7988.
59. P. K. Lam, M.L. Cohen, G. Martinez, *Phys. Rev. B*, 35 (1987) 9190.
60. Y. Al-Douri, H. Abid, H. Aourag, *Mater. Chem. Phys.*, 87 (2004) 14.
61. Y. Z. Zhu, G. D. Chen, H. Ye, A. Walsh, C. Y. Moon, S-H. Wei, *Phys. Rev. B*, 77 (2008) 245209.
62. A. A. Odeh, Y. Al-Douri, C. H. Voon, R. Mat Ayub, S. C. B. Gopinath, R. A. Odeh, M. Ameri, A. Bouhemadou, *Electrochim. Acta*, 184 (2017) 2211.